Article
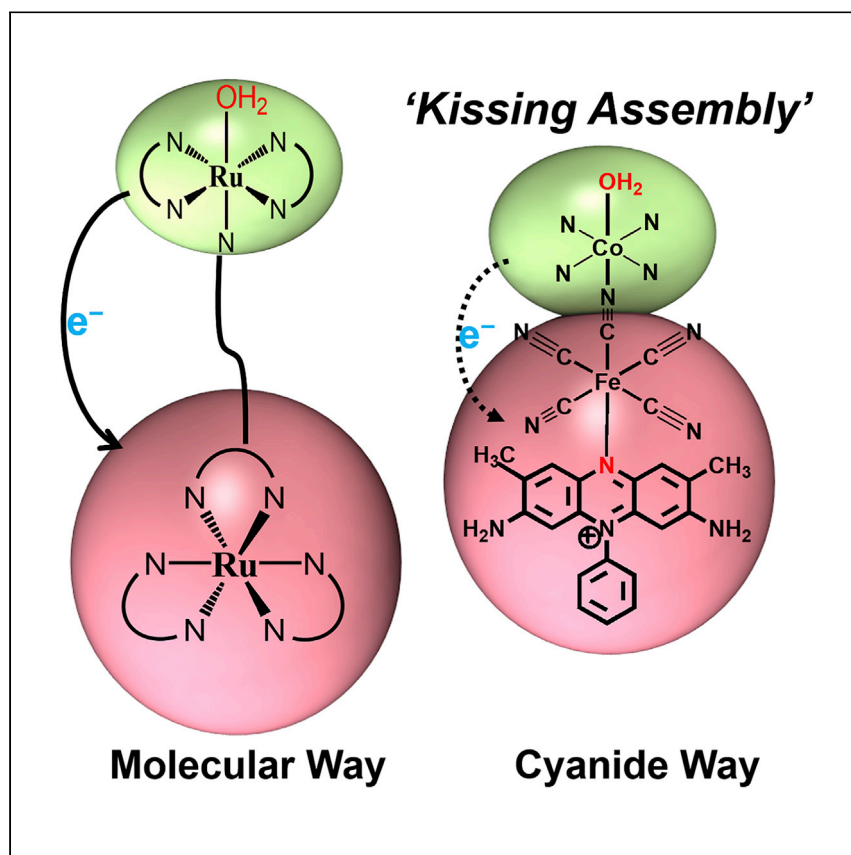
Pushing the limits in photosensitizer-catalyst interaction via a short cyanide bridge for water oxidation

'Kissing Assembly'

Molecular Way   **Cyanide Way**

The realization of high-performance and stable precious-metal-free photoanodes is one of the bottlenecks in dye-sensitized water splitting. Here, Ghobadi et al. report an extendable synthetic approach based on cyanide chemistry to maximize mutual coupling between the photosensitizer and the catalyst, producing a high-performance, stable photoanode.

Turkan Gamze Ulusoy Ghobadi, Amir Ghobadi, Merve Demirtas, ..., Engin Durgun, Ekmel Ozbay, Ferdi Karadas

gamze.ulusoy@bilkent.edu.tr (T.G.U.G.)
karadas@fen.bilkent.edu.tr (F.K.)

HIGHLIGHTS

Using cyanide chemistry, a Ru-free water oxidation photoanode is demonstrated

The photoanode shows stable performance under long-term light irradiation

At 1.23 V_{RHE}, a photocurrent density as high as 1,300 $\mu A\ cm^{-2}$ is achieved

Article

Pushing the limits in photosensitizer-catalyst interaction via a short cyanide bridge for water oxidation

Turkan Gamze Ulusoy Ghobadi,[1,8,*] Amir Ghobadi,[2,3] Merve Demirtas,[4] Ruby Phul,[5] Elif Akhuseyin Yildiz,[6] Halime Gul Yaglioglu,[6] Engin Durgun,[1] Ekmel Ozbay,[2,3,7] and Ferdi Karadas[1,5,8,*]

SUMMARY

The realization of high-performance, precious-metal-free, stable, and robust photoanodes for water oxidation is one of the bottlenecks for dye-sensitized water splitting. Herein, we integrate an organic photosensitizer, which absorbs visible light above 500 nm, with a Prussian blue (PB) network to sensitize a visible-light-absorbing semiconductor, WO_3. Through comprehensive steady-state and ultrafast transient absorption studies, we show that the coupling of a photosensitizer to a catalyst through a short cyanide bridging group in a PB structure generates appropriate energy levels for an efficient charge transfer from the photosensitizer to the visible-light-absorbing semiconductor. The photoanode retains its structural integrity and high photoelectrochemical activity for at least 2 h of solar irradiation under mildly acidic conditions (pH 3), which reaches around 1.30 mA/cm^2 at 1.23 V_{RHE}. This work provides a simple recipe with a toolbox that can be extended to a variety of organic photosensitizers and semiconductors.

INTRODUCTION

To date, precious-metal-based complexes are the major ingredients of almost all photosensitizers (PSs), water oxidation catalysts (WOCs), and thus PS-WOC assemblies.[1,2] Besides their high cost, poor long-term stability of ruthenium-based assemblies limits their further upscaling for potential industrial usage. Despite intensive studies to improve the stability of these systems,[3–6] their poor long-term performance is still a major challenge. Another pathway is to explore earth-abundant and stable alternatives for ruthenium. In this regard, three-dimensional (3D) transition-metal complexes[7] and metal-free organic dyes[8] have been the subject of a decade-long investigation. Among 3D transition metals, "iron hits the mark."[9,10] Despite major breakthroughs on the iron chromophores, including 92% light-to-electron conversion yield,[11] nanosecond charge-transfer excited-state lifetime,[12] and room-temperature photoluminescence,[13] there has been no successful attempt at developing an iron-sensitized water oxidation photoanode, mainly due to the lack of a facile synthetic pathway. On the other hand, aromatic macrocycles, including porphyrin and phthalocyanines, have been the pioneer organic chromophores to replace ruthenium analogs.[8] Their poor carrier transport and sluggish interfacial dynamics, however, had to be compensated with Ir- or Ru-based complexes as WOCs.[4,14–16] Even in this case, their photocurrents stayed below 100 μA/cm^2 with a nominal half-life of tens of minutes. Although precious-metal-free water oxidizing dye-sensitized photoanodes were recently prepared by utilizing a perylene diimide derivative as the PS and CoO_X as the WOC, the assembly suffered from severe

[1]UNAM—National Nanotechnology Research Center, Institute of Materials Science and Nanotechnology, Bilkent University, Ankara 06800, Turkey

[2]Department of Electrical and Electronics Engineering, Bilkent University, Ankara 06800, Turkey

[3]NANOTAM—Nanotechnology Research Center, Bilkent University, Ankara 06800, Turkey

[4]Department of Physics, Kafkas University, 36100 Kars, Turkey

[5]Department of Chemistry, Bilkent University, Ankara 06800, Turkey

[6]Department of Engineering Physics, Faculty of Engineering, Ankara University, 06100 Ankara, Turkey

[7]Department of Physics, Bilkent University, Ankara 06800, Turkey

[8]Lead Contact

*Correspondence:
gamze.ulusoy@bilkent.edu.tr (T.G.U.G.),
karadas@fen.bilkent.edu.tr (F.K.)

https://doi.org/10.1016/j.xcrp.2020.100319

electron-hole recombination due to the undesired/uncontrolled growth of the catalyst on the semiconductor surface, resulting in a dramatic decline in the photocurrent and a poor long-term stability.[17,18]

We recently demonstrated stable and entirely earth-abundant PS-WOC assemblies via coordination of a pentacyanoferrate group to pyridyl-containing organic chromophores.[19,20] Although the photoanode is stable with an excited-state lifetime in nanosecond scales, the performance falls behind the efficient Ru-based systems due to the unfavorable band alignment between the dye and the relatively wide bandgap TiO_2.[20] The lack of an efficient component that can absorb light in the visible region, particularly above 500 nm, is also responsible for the relatively poor efficiency.

Herein, we move one step forward and build a cyanide-based water oxidation photoanode, which incorporates a visible-light-absorbing semiconductor and an organic photosensitizer that absorbs light above 500 nm. Although common PS-WOC assemblies require the utilization of a relatively long organic group to connect a PS to a WOC, we employ a short cyanide ligand as the bridging group to mediate the charge transfer between these units. In the proposed architecture, an organic PS, safranin O (absorption bandwidth: 400 nm < λ < 550 nm) is implemented to a CoFe PB structure [CoFe–SF] to improve its stability and tune its energy levels. It is then coated over the visible-light-absorbing WO_3 nanoplates (λ < 440 nm) to build the dye-sensitized photoanode [CoFe–SF]/WO_3. Besides its narrow bandgap, the choice of WO_3 stems from the desirable energetic position of its conduction band (CB). The elegantly designed PS-WOC assembly offers highly efficient water oxidation through (1) harvesting below bandgap photons and (2) acting as an energetically engineered WOC for the WO_3 host. At 1.23 V_{RHE} bias, 1.30 mA/cm^2 photocurrent is achieved by [CoFe–SF]/WO_3 while the maximum photo-dark current difference reaches to a remarkable value of 1.77 mA/cm^2 at 1.8 V_{RHE} and pH 3.

RESULTS AND DISCUSSION

Structural analysis

The surface texture of the metal oxide, as the electron extraction layer, is of great importance. Unlike nanoparticles, porous designs that impose a "random walk" direction for electron transfer, anisotropic one-/two-dimensional (1D/2D) structures promote the "direct transfer."[21] Thus, single-crystalline WO_3 nanoplates are preferred to maximize the collection efficiency of the carriers and synthesized using a hydrothermal growth technique. An *in situ* preparation of CoFe PB layer is chosen to improve physical interaction between WO_3 and [CoFe–SF] layer. WO_3 is first sensitized with a pentacyanoiron coordinated to safranin complex, [FeSF] complex, to afford a [Fe-SF]/WO_3 heterojunction (Figures 1A and 1B). Finally, *in situ* coordination of Co^{2+} ions leads to the formation of a bulk PB layer on the semiconductor surface, [CoFe–SF]/WO_3 photoanode (Figure 1C). The details on materials synthesis and the structural characterizations are provided in Scheme S1, Table S1, and Figures S1–S6. In the molecular perspective, [CoFe–SF] consists of organic chromophore groups ([SF]) connected to catalytic cobalt sites through Fe(CN)$_5$ groups (Figure 1D). The absence of diffraction peaks for a PB structure and the presence of characteristic peaks for the organic group and a Fe–CN–Co coordination mode in the infrared spectrum suggest that [CoFe–SF] layer on WO_3 can be described as an amorphous non-periodic bulk structure as expected.[19,20,22]

Photoelectrochemical performance

Photoelectrochemical (PEC) studies are performed on bare WO_3, [CoFe]/WO_3, and the [CoFe–SF]/WO_3 photoanode in a three-electrode setup to understand the role of
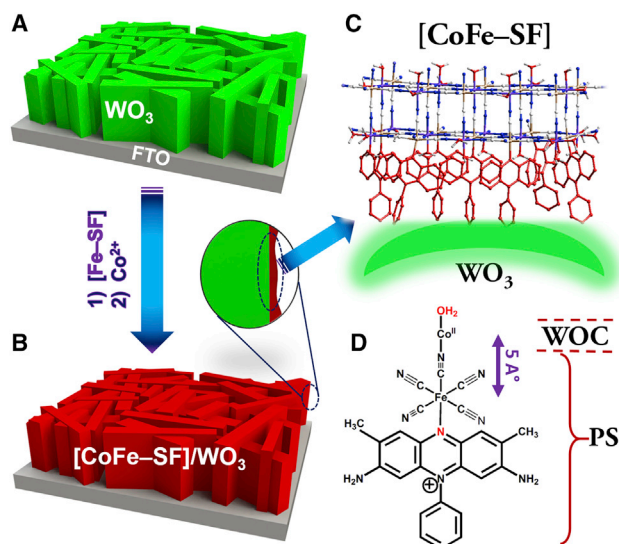
Figure 1. Schematic Illustration of the Formation Process of Dye-Sensitized Photoanode and Structural Design for O_2 Production from water

(A and B) Illustration of (A) bare WO_3 nanoplates on FTO-coated glass and (B) the CoFe Prussian blue (PB) modified dye-sensitized WO_3 photoanode (WO_3/[CoFe–SF]). It is a two-step process: first, WO_3 nanoplates are immersed into Fe-bonded Safranin dye ([Fe–SF]) solution and then *in situ* drop casting a solution of Co^{2+} ions to form [CoFe–SF] bulk structure. The electrode color changes from green to reddish.

(C) The structure of WO_3/[CoFe–SF] where the CoFe PB assembly forms an extended bulk network.

(D) The role of each component in the dye-sensitized photoanode. In this molecular fragment, the [Fe–SF] is the PS part and Co site acts as the WOC. Moreover, CoFe PB component serves as a strongly electron-donating group for SF. The cyanide bridge has a length of around 5 Å. Only a molecular fragment of the extended structure is displayed, and the coordination environment of cobalt site is omitted for clarity.

See also Scheme S1.

each layer (Figure 2A). Pulsed linear sweep voltammetry (LSV) profiles are measured under AM1.5G illumination with 435 nm and 495 nm cutoff filters. Under solar irradiation, the maximum photo-dark current difference of 1.77 mA/cm^2 is achieved at 1.8 V_{RHE} for [CoFe–SF]/WO_3, although it is only 1.14 mA/cm^2 and 0.9 mA/cm^2 for WO_3 and [CoFe]/WO_3 electrodes, respectively. When an excitation above λ > 435 nm is used to largely suppress the photoresponse of WO_3, all LSVs exhibit similar profiles, although that of [CoFe–SF]/WO_3 is more prominent than other electrodes. The use of a 495-nm cutoff filter, however, completely deactivates the photoresponse of WO_3 and WO_3/[CoFe], although the [CoFe–SF]/WO_3 retained its photocurrent generation (see Figure 2B).

Indeed, a 495-nm cutoff filter was intentionally used to fully deactivate the WO_3 photoresponse. The activity with this filter also rules out the possible decomposition of the Prussian blue assembly to an active catalytic system because a possible charge transfer mechanism involving the absorption of photons by WO_3 cannot operate under these conditions. A chromophore should thus be responsible for the photocurrent obtained. Based on Figure 2C, the incident photon-to-current conversion efficiency (IPCE) for the bare sample is extended up to 460 nm, which is in line with the above-filtered LSV results. The same spectral response is observed for [CoFe]/WO_3, however, with lower efficiencies. The IPCE profile for [CoFe–SF]/WO_3 differs. For above-bandgap photons, where both dye and semiconductor are responsive, the IPCEs are improved, although in longer ranges (where only dye is
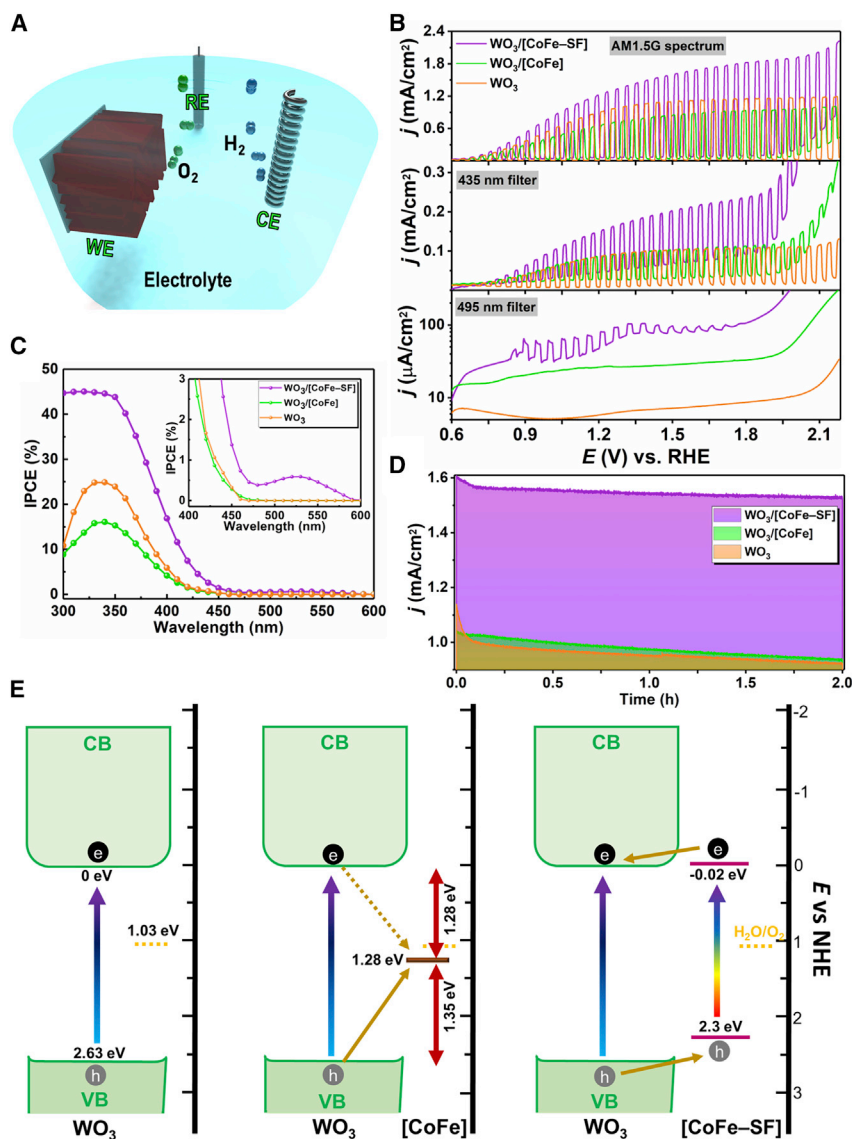
Figure 2. Photoelectrochemical (PEC) performance of WO$_3$/[CoFe–SF] for water oxidation

(A) 3D schematic diagram of the three-electrode cell used for PEC water splitting measurements.

(B) Pulsed linear sweep voltammetry (LSV) curves performed for WO$_3$, WO$_3$/[CoFe], and WO$_3$/[CoFe–SF] electrodes under white-light illumination (top) and with 435-nm (middle) and 490-nm (bottom) cutoff filters. In all three conditions, the dyad-sensitized photoanode has much stronger response compared to bare and catalyst case. For 490-nm cutoff case, the WO$_3$ and WO$_3$/[CoFe] photoanodes have no photoresponse although the WO$_3$/[CoFe–SF] electrode shows photocurrent response.

(C) IPCE spectra for the same photoanodes at 1.23 V$_{RHE}$. The inset shows a magnified image of the 400–600 nm range. The IPCE results in visible range originates from the [CoFe–SF].

(D) Chronoamperogram profiles of different photoanodes for 2-h solar illumination at 1.23 V$_{RHE}$. This test confirms the stability of the photoanode upon solar irradiation.

(E) Schematic band energy alignment and carrier dynamics for all three photoanodes between different interfaces and water oxidation levels. The energetic position of the PB layer in WO$_3$/[CoFe] case has been significantly modified due to its connection to the dye molecule. This modification provides a proper band alignment for hole transport toward the water oxidation process.

See also Figures S7–S10.

active), the photocurrent is extended up to 600 nm. The remarkable improvement in the IPCE is also reflected in the photocurrent achieved in a long-term experiment (Figure 2D). The catalytic behavior of [CoFe–SF] is proven by Nyquist plots obtained using electrochemical impedance spectroscopy (EIS) under solar irradiation at 1.23 V_{RHE} (Figure S7). The semicircle radius, representing the charge transfer resistance, shrinks for [CoFe–SF]/WO$_3$, due to the alleviation of the interfacial charge dynamics. Similar behavior has previously been observed for PS-WOC assemblies.[23,24] It is noteworthy that, without Co coordination, i.e., [Fe–SF]/WO$_3$, the charge resistance is much larger (Figure S8), and consequently, the photocurrent is significantly lower with poor stability (Figure S9). It should be noted that [Fe–SF], just the chromophore itself, is molecular although [CoFe–SF], chromophore-catalyst assembly, is bulk. A decline in the photocurrent response is observed for [Fe–SF] case as expected from a molecular chromophore (see Figure S9). WO$_3$/[CoFe–SF] photoanode, however, maintains a relatively constant photocurrent response throughout a 2-h experiment, as shown in Figure 2D. Therefore, the formation of the CoFe PB structure is essential for an efficient water oxidation process. Band alignments were further extracted by combinational analysis of cyclic voltammetry (CV), Mott-Schottky, and absorption profiles (Figures S14–S18). The band alignments are depicted in Figure 2E. For [CoFe]/WO$_3$, the PB is positioned at almost equal energetic distances to the CB and valance band (VB) of WO$_3$, mediating the electron/hole recombination (electrons from CB and holes from VB). Therefore, PB serves as a trapping center rather than a WOC, which reduces the photocurrents further as the PB loading increases (Figure S10). On the other hand, for [CoFe–SF]/WO$_3$, both photocurrents are enhanced significantly and absorption capacity is extended to longer wavelengths because the energy levels are reorganized due to the close interaction between the safranin unit and PB structure.

Photoelectrochemical and photocatalytic stability

Moreover, the structural integrity of the assembly governs the long-term stability of the design. To scrutinize this issue, we used transmission electron microscopy (TEM) and X-ray photoelectron spectroscopy (XPS) analysis on both pristine and post-catalytic (after 2-h-long chronoamperometry [CA] experiment) photoelectrodes. High-resolution TEM (HR-TEM) analysis suggests the presence of similar [CoFe–SF] layers (denoted as Prussian blue analogue [PBA]) in both the pristine and post-catalytic photoelectrodes, confirming their long-term stability. These PBA shell layers are grown both as continuous and island-like regions on the surface of WO$_3$ nanoplates in pristine and post-catalytic WO$_3$/[CoFe–SF] photoelectrodes (Figures 3A–3B). HR-TEM images also reveal that the WO$_3$ component exhibits a crystalline phase with interplanary spacing of 0.37 nm corresponding to (200) plane of the monoclinic phase of WO$_3$ structure, as shown in Figure 3A, right. Further confirmation on the existence of a PBA layer on the WO$_3$ surface, on a large scale, is achieved by using a TEM-EDX line scan and area energy dispersive X-ray (EDX) analysis. As shown in Figure S11, both pristine and post-catalytic samples contain a PBA layer on their surfaces. Finally, XPS analysis is employed to examine the stability of the photoanode after the CA experiment. As expected, an enhancement in Co^{3+} and Fe^{3+} signals is observed in the post-catalytic sample, which indicates that cobalt and iron sites are partially oxidized during the water oxidation process (see Figure S12). The fully oxidized form of cobalt (Co$_3$O$_4$) was, however, not observed, which indicates that the CoFe PB layer retains its chemical stability under photoelectrochemical conditions. A photocatalytic degradation experiment is performed to further prove the stability of [CoFe–SF] bulk assembly. Here, both the [SF] and [CoFe–SF] are exposed to solar light (1 sun; 100 mW/cm^2) for 500 min in the presence of WO$_3$ powder (~2 mg), and the change in the dye absorption peak as a function of exposure
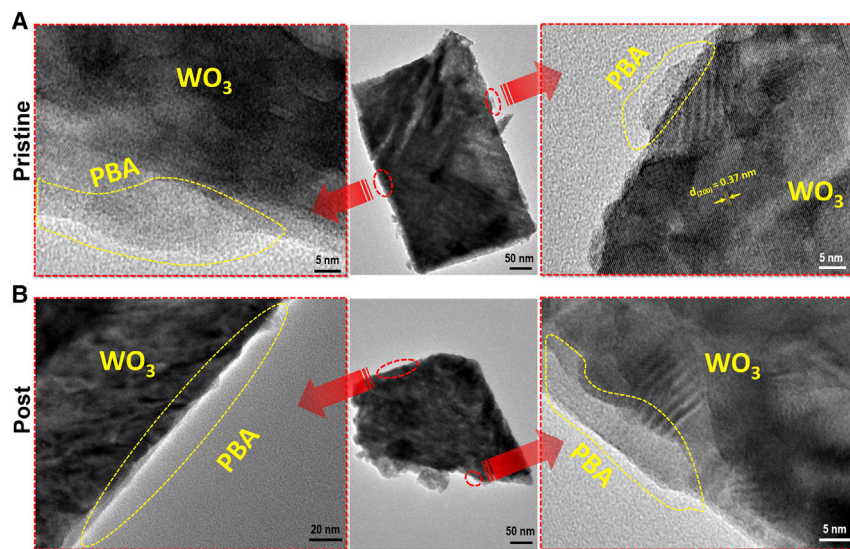
Figure 3. TEM and HR-TEM analysis of pristine and post-catalytic WO₃/[CoFe–SF] sample

PBA region is shown by yellow color dashed lines.

(A) Pristine WO₃/[CoFe–SF] sample; (left) the HR-TEM image from the WO₃-PBA interface, indicating the formation of an ultrathin PBA extended network on the WO₃ surface; (middle) TEM image of an individual pristine WO₃ nanoplate sensitized with [CoFe–SF] assembly; and (right) HR-TEM of WO₃/[CoFe–SF], showing the formation of island-like PBA shell layers on the WO₃ surface. Based on this HR-TEM image, the WO₃ semiconductor has a single crystalline phase with an interplanar spacing of 0.37 nm, which is consistent with its monoclinic phase.

(B) Post-WO₃/[CoFe–SF] sample; (left) HR-TEM image from the WO₃-PBA interface, showing the formation of both continuous and island-like PBA layer; (middle) TEM image of an individual nanoplate after chronoamperometry (CA) experiment; and (right) HR-TEM image from the WO₃-PBA interface, showing the existence of a uniform PBA shell layer after CA experiment.

time to light was investigated (see Figures 4A–4D). At the end of this experiment, the color of [SF] solution fades, and its characteristic absorption bands disappear as expected.[25] On the other hand, [CoFe–SF] exhibits a slight decrease in its spectral response even in the primitive design, in which the [CoFe–SF] and WO₃ powder samples are mixed (note that an *in situ* synthesis is employed to improve the stability and physical interaction between WO₃ and [CoFe–SF]). A similar response in PS-semiconductor designs has previously been reported, in which the poor stability of the architecture is attributed to the unstable reduced state formed upon an electron transfer from the PS to the semiconductor.[26,27] Therefore, the photocatalytic degradation experiment together with the aforementioned TEM, XPS, long-term CA measurements, and IPCE response, particularly in the 480- to 600-nm region, indicate the critical role of the bulk PB structure on the stability and the performance of the photoanode. Finally, a CA experiment at 1.23 V_{RHE} (at pH 3) was performed with a gas-tight cell and the amount of photogenerated O_2 was recorded by an O_2 probe. A Faradaic efficiency of approximately 75.3% (as explained in Figure S13) indicates that the photocurrent response is mainly originated from the water oxidation process.

Steady-state and transient optical analysis

In the next step, optical studies are performed to understand the effect of PB structure on the energy levels of the photosensitizers. Although all dye complexes have similar absorption and fluorescence profiles (Figure 5A), a gradual blue shift occurs from [SF] to [Fe–SF] and to [CoFe–SF], which is also evident on their fluorescence colors, upon white and green light excitation (Figure 5B). The behavior of [SF] and
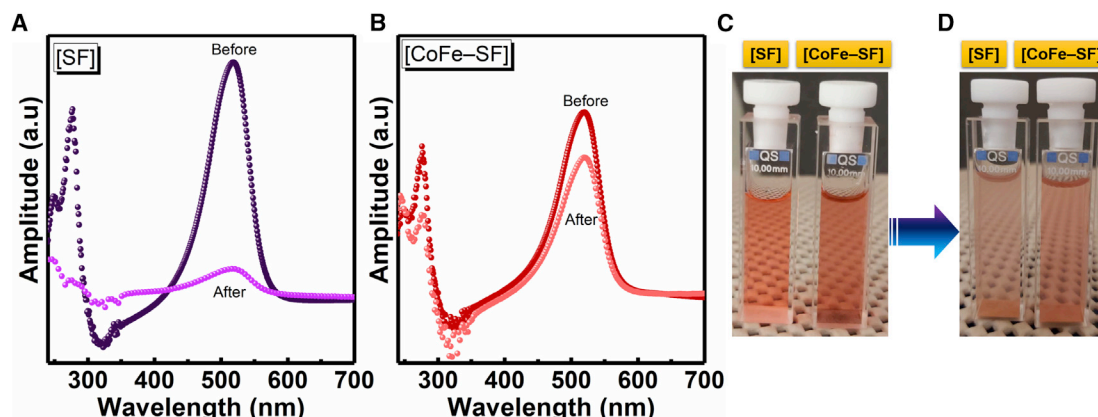
Figure 4. Photocatalytic degradation test
(A and B) Photocatalytic degradation measurement, absorption profiles before and after 500 min solar light exposure of the (A) [SF] and (B) [CoFe–SF] aqueous solutions in the presence of the same amount of WO$_3$ powder.
(C and D) The optical image showing the related color change (C) before and (D) after the photocatalytic experiment for both solutions.

[CoFe-SF] upon broadband illumination, where a wide range of optical excitations is possible, indicates that they exhibit different excited state energetic levels. This is the origin of the fluorescence color difference between the two complexes. Electronic transitions in ultra-short timescales are tracked to elucidate this difference. Time-resolved fluorescence (TRF) spectroscopic studies are performed on both solutions and photoanodes with a 495-nm excitation. The decay dynamics in photoanodes are much faster than those in solutions, due to the existence of new recombination pathways induced by WO$_3$ (Figure 5C). That is why solutions exhibit a single decay rate (lowest unoccupied molecular orbital [LUMO] → highest occupied molecular orbital [HOMO] transition), although photoanodes have multiple exponential rates (multiple relaxation routes). Moreover, the faster decays in [Fe–SF]/WO$_3$ and [CoFe–SF]/WO$_3$ are a sign of efficient injection dynamics (Figure 5D). The excited electrons are transferred into WO$_3$ CB and back-recombine with holes in the HOMO level. It is thus clear that energy levels are reconstructed with the incorporation of a PB layer.

Computational studies and transient absorption spectroscopy
Ab initio electronic structure calculations based on density functional theory with periodic boundary conditions were employed to explore this modification at the molecular level (Figures 6A–6C). In line with the experimental findings (Figure 6A), *ab initio* calculations suggest that the integration of the [SF] group to the PB structure gradually widens the HOMO-LUMO gap. The nature of electronic states is also altered with the coordination of cobalt ions. The HOMO of [CoFe–SF] is distributed over the iron site and organic ligand although that of [Fe–SF] is fully localized only on the iron site. On the other hand, all of the excited states in [Fe–SF] are mostly ligand centered (LC) in character, which mediates efficient metal-to-ligand charge transfer (MLCT). For [CoFe–SF], the LUMO is localized on the cobalt site (metal-to-metal charge transfer [MMCT]) and LUMO-i (i ≥ 1) are LC (ideal for MLCT process). The weak band at ~630 nm is assigned to the MMCT process (Fe^{III}-CN-Co^{II} ⇌ Fe^{II}-CN-Co^{III}) as it is depleted with the gradual addition of an oxidizing agent (1 M aqueous Na$_2$S$_2$O$_8$) to oxidize metal ions to their +3 oxidation states (Figures 6D–6G). The MMCT band is much weaker compared to the MLCT one, which suggests that MLCT dominates over the MMCT during the charge transfer process. Transient absorption (TA) spectroscopy is used to probe the electronic transitions in femtosecond transient scales. The TA spectra of WO$_3$/[SF] and WO$_3$/[Fe–SF], in different
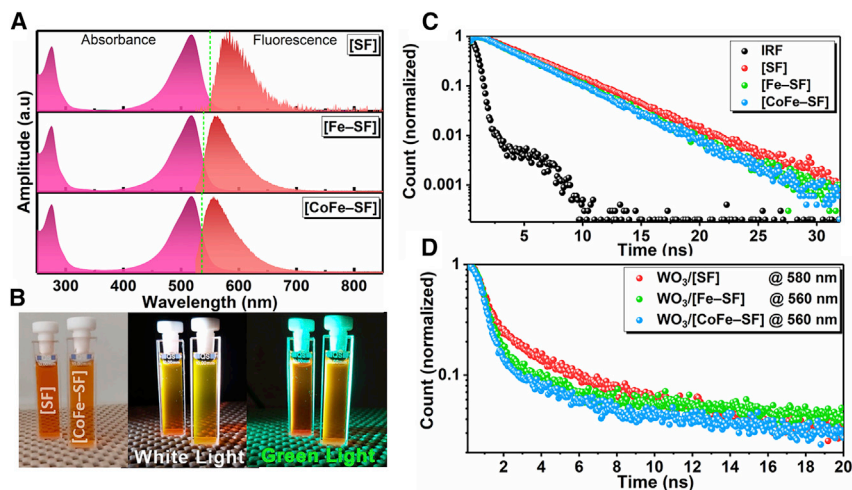
Figure 5. Steady-state and transient optical measurements

(A) Absorption and fluorescence spectra (with an excitation of 520 nm) of the [SF], [Fe–SF], and [CoFe–SF] solutions (0.02 mM in MeCN solutions). The optical band gap of different complexes is defined by the intersection point of absorption and fluorescence spectra.

(B) [SF] and [CoFe–SF] solutions in dark and their fluorescence under white and green light illuminations.

(C and D) The TRF spectra of (C) the dye solutions and (D) photoanodes upon 495-nm excitation. The probe signal for each electrode is shown in the legend.

See also Figure S14.

time delays, resembles that of their solutions with two main features: a negative signal attributed to ground-state bleaching (GSB) and a positive response raised from excited-state absorption (ESA) (Figures 7A–7C and S19). The ESA signal followed with a sluggish GSB for WO$_3$/[Fe–SF] decays much faster (within the first 100 ps delay) than WO$_3$/[SF]. However, the ESA peak vanishes in the first 200-fs time delays for WO$_3$/[CoFe–SF], and here, the decay of the ESA feature without the loss of GSB amplitude is a signature of electron injection (Figure 7C), as explained in previous studies.[28–30] This can be further proven by looking at the band alignments between WO$_3$ and different dye complexes of [SF], [Fe-SF], and [CoFe–SF], as shown in Figures 7D–7F. A more favorable band alignment for WO$_3$/[CoFe–SF] is the reason for the efficient injection dynamics. Therefore, the PB extended network not only acts as a WOC but also modifies the electronic level alignment between semiconductor host and dye absorber. Due to proper band alignment, the selective isolation of photoexcited electrons and holes is provided, and this leads to high water oxidation activity. Figure 7G schematically summarizes the responsible steps for photoelectrochemical water oxidation using the proposed dye-sensitized photoanode.

In this work, we present a strategy to push the limits of the interaction between the PS and the WOC for the development of a high-performance, precious-metal-free, dye-sensitized water oxidation photoanode. In this architecture, an organic photosensitizer that absorbs visible light above 500 nm, an iron relay group, and a cobalt water oxidation catalytic site were connected through short cyanide groups, which promotes electronic interaction between these components. Ultrafast transient absorption and computational studies suggest the mixing of electronic states of organic PS, iron, and cobalt groups to reorganize the excited states for enhanced e$^-$ transfer during the photoelectrochemical process. This strong interaction is reflected also in the stability and activity of the dye-sensitized photoanode, which is
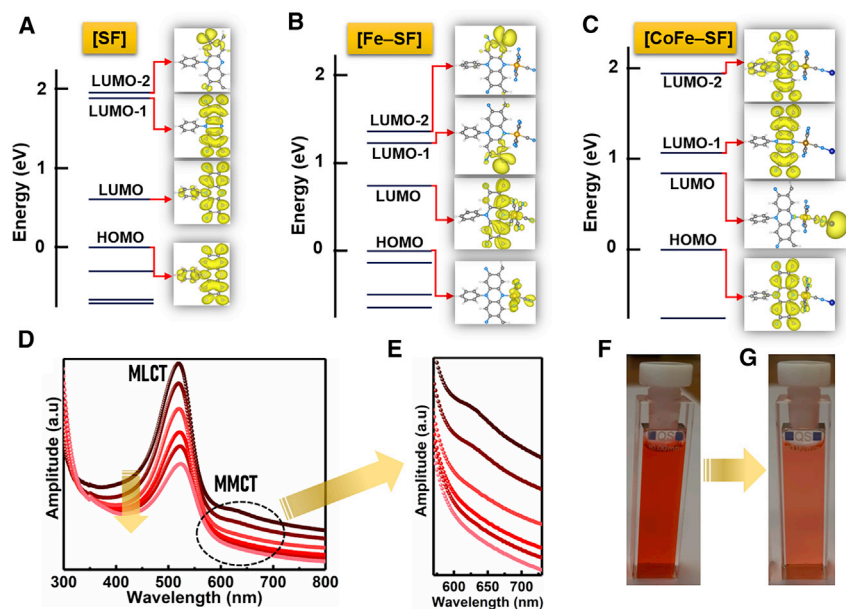
Figure 6. Theoretical first-principle calculations and metal-to-metal charge transfer feature

(A–C) HOMO and LUMO energy levels with the electron clouds for all 3 components of (A) [SF], (B) [Fe–SF], and (C) [CoFe–SF], calculated with PBC-density functional theory (DFT) using hybrid functionals.

(D) Changes observed in the ultraviolet-visible (UV-Vis) spectrum of an aqueous solution of the [CoFe–SF] complex with the incremental addition of 1 M aqueous $Na_2S_2O_8$ solution.

(E) The magnified image shows the presence of the MMCT state between the wavelengths of 550 and 750 nm, which infers the effective depletion of the 3+ states in the same complex.

(F and G) Related color change in the solution (F) before and (G) after the experiment.

built by the Ru-free PS-WOC assembly coated over a visible light-absorbing semiconductor, WO_3. A photocurrent density of 1.3 mA/cm^2 can be achieved at 1.23 V_{RHE} with an efficient photon-to-electron conversion up to 600 nm for at least 2 h of illumination. In conclusion, we provide an easy-to-assemble pathway to develop earth-abundant, efficient, and robust dye-sensitized photoelectrodes through a cyanide-based synthetic approach. Given the diversity and simplicity of the approach, more examples will clearly follow to further explore cyanide-based dye sensitization.

EXPERIMENTAL PROCEDURES

Resource availability

Lead contact
Further information and requests for resources and reagents should be directed to and will be fulfilled by the lead contact, T. Gamze Ulusoy Ghobadi (gamze. ulusoy@bilkent.edu.tr).

Materials availability
This study did not generate new unique reagents.

Data and code availability
The data supporting the findings of this study are available from the lead contact on request.

Synthesis of pentacyanoferrate-coordinated safranin, [Fe–SF]
Sodium aminopentacyanoferrate, $Na_3[Fe(CN)_5NH_3]\cdot3H_2O$, [Fe-NH$_3$] precursor was synthesized according to our previously reported procedure.[19,22] The compounds
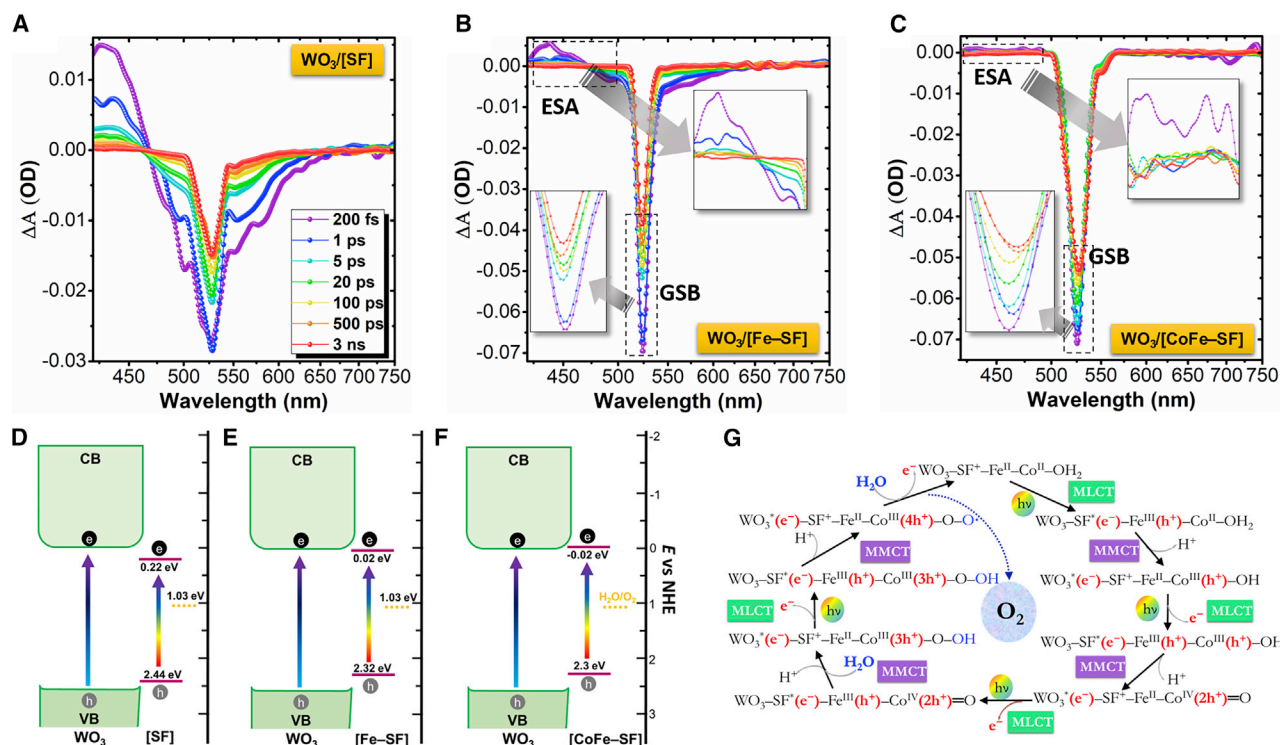
Figure 7. Transient absorption characterizations, energy band alignment, and involved water oxidation mechanism
(A–C) TA spectra of the electrodes upon 520 nm (pump) excitation at different pump-probe time delays for (A) WO$_3$/[SF], (B) WO$_3$/[Fe–SF], and (C) WO$_3$/[CoFe–SF].
(D–F) Schematic representation of band alignments for (D) WO$_3$/[SF], (E) WO$_3$/[Fe–SF], and (F) WO$_3$/[CoFe–SF] photoanodes.
(G) Proposed molecular mechanism of the PEC water oxidation for [CoFe–SF].
See also Figures S17–S19 and Table S2.

[Fe–SF] and [CoFe–SF] were synthesized by adopting a similar synthetic approach according to our previous report.[20] Na$_3$[Fe(CN)$_5$NH$_3$]·3H$_2$O (0.5 mmol) was dissolved in a sufficient amount of water, giving a bright yellow solution followed by the dropwise addition of ~10 mL ethanolic solution of [SF] (0.5 mmol). The color of the [SF] compound changed from pink to dark brown. The reaction mixture was left under constant stirring at room temperature overnight. The pink-brown concentrated solution was centrifuged at 6,000 rpm for 20 min in cold ethanol to get the purified product. Finally, the precipitate was collected and dried in an oven at 30°C–40°C overnight.

Synthesis of cobalt pentacyanoferrate-coordinated safranin, [CoFe–SF]
[Fe–SF] compound (10 mg; 18 μmoles) was dissolved in MeCN and 1 eq. Co(NO$_3$)$_2$ in EtOH was added dropwise to the [Fe–SF] solution. The resulting dark brown solution was left under stirring for 2 h at room temperature. To get a purified product and remove soluble unreacted species, the suspension was centrifuged at 6,000 rpm for 20 min. The precipitate was washed with acetone until the desired purity was obtained. The final product was dried in an oven at 35°C for 1 day.

Synthesis of WO$_3$ nanoplate arrays
WO$_3$ nanoplate arrays, noted as WO$_3$ for short, were prepared by modifying the hydrothermal synthesis as previously described elsewere.[31,32] In detail, 231 mg of Na$_2$WO$_4$ as a tungsten resource dissolved in 30 mL distilled water. Then, 10 mL of 3M HCl was added dropwise to the solution under constant stirring to form tungsten acid (H$_2$WO$_4$). After being stirred for 30 min under ambient conditions, 0.2 g

$(NH_4)_2C_2O_4$ was added as a structure-directing agent. To a 70 mL of solution, a total 30 mL deionized water was added and stirred vigorously further for 30 min. The precursor solution was transferred to a Teflon-lined stainless-steel autoclave (capacity of 100 mL) with an fluorine-doped tin oxide FTO conducting side against the wall. In advance, FTO glasses (1 cm × 6 cm) are cleaned sufficiently in sonication baths in DI water, acetone, and ethanol in sequence, each for 15 min, and then dried by N_2 flow. The hydrothermal reaction was carried out at 120°C for 18 h and then it was naturally cooled to room temperature. Finally, the sample was thoroughly rinsed with DI water to remove the residual solvent and calcined at 450°C for 2 h in a ceramic furnace.

$WO_3/[CoFe]$ electrode

The Prussian blue coatings were prepared according to the previously reported procedure with slight modifications.[33] In detail, WO_3 electrodes soaked in $[K_3Fe(CN)_6]$ (0.02 M) in Milli-Q water solution for 1 min at room temperature. The samples were then rinsed with water to remove the non-adsorbed Fe^{2+} ions. Once the substrate was completely dried, the electrode was immersed in $Co(NO_3)_2.6H_2O$ solution (0.04 M) for 1 min. Then, the electrode surface was washed with distilled water to remove the excess Co^{2+} ions over the film. This process was repeated at least two times to complete the full coverage of Prussian blue analog. Finally, the $WO_3/$ [CoFe] electrode was left to dry at room temperature.

$WO_3/[CoFe–SF]$ electrode

WO_3 electrodes soaked in [Fe–SF] (1.4 mM) in MeCN solution for 24 h at room temperature. The samples were then rinsed with MeCN to remove any non-adsorbed dye molecules. Once the substrate was completely dried, ∼500 μL of $Co(NO)_3$ solution (0.04 M) was drop cast onto the $WO_3/[Fe–SF]$ electrode. Then, the slide was washed with distilled water to remove the excess Co^{2+} ions over the film. This process was repeated two times to complete the full coverage of Prussian blue analog. Finally, the $WO_3/[CoFe–SF]$ electrode was left to dry at room temperature.

Materials characterization

Scanning electron microscopy (SEM) (FEI – Quanta 200 FEG) was used to characterize the morphology and operated at 15 kV.

A TEM (Tecnai G2-F30; FEI), operating at 200 kV, was used to examine the surface characteristics of the samples. TEM samples were prepared by scratching the coated nanoplates from the FTO samples and then dispersed in ethanol and finally drop casted on a holey carbon-coated copper grid.

Powder X-ray diffraction (PXRD) has been carried out by Panalytical X'pert Multi-Purpose to identify the phase structure of the obtained sample, and the patterns have been collected in the range of $2\theta = 15°–70°$ using Bragg-Brentano geometry (Cu Kα radiation; $\lambda = 0.15418$ nm). The spectra (Figure S2) reveal that the diffraction peaks match well with the powder X-ray diffraction pattern for monoclinic phased tungsten oxide (JCPDS card no. 00-024-0747) with cell parameters a = 7.2970 Å and c = 7.6880 Å.

Fourier-transform infrared spectroscopy (FTIR) spectra were measured using a Bruker ALPHA Platinum-ATR spectrometer in the wavenumber range 4,000–400 cm^{-1}.

Raman spectra were recorded in the 4,000–300 cm^{-1} spectral region, with a WITecAlpha 300S scanning near-field optical microscope with Raman module, using a 532-nm laser wavelength, 1 mW power, and 20× objective, with a 5-s recording time and 20 scans.

XPS (Thermo Fisher Scientific; Al K-Alpha radiation; hυ = 1486.6 eV) measurement was also performed at survey mode by operating a flood gun for surface charge neutralization with 30 eV pass energy and 0.1 eV step size, and it was performed for determining the elemental analysis. Because charge compensation may not be sufficient in eliminating all of the surface charge, the peak positions correction was calibrated by referencing the C1s peak position (284.8 eV) and shifting other peaks in the spectrum accordingly. To understand the chemical bonding states, the deconvolution of high-resolution XPS spectra over Fe2p and Co2p was conducted for all of the samples, and the results are summarized in Table S1.

Photoelectrochemical measurements

A Gamry Instruments Interface 1000 Potentiostat/Galvanostat was used for all (photo)electrochemical measurements. The standard three-electrode electrochemical cell configuration was performed using WO_3 photoanodes on FTO substrates with an exposed area of 2 cm^2, a Pt mesh counter electrode, and Ag/AgCl (3 M KCl) reference electrode. All of the calculations were based on the geometric surface area unless specified otherwise.

Photoelectrochemical studies on photoanodes (WO_3, WO_3/[CoFe], and WO_3/[CoFe–SF]) have been performed using a 0.1 M Na_2SO_4 (pH 3 at 25°C), and before each measurement, the electrolyte solution was saturated with N_2 gas (99.999% purity) for 30 min to remove the dissolved O_2 gas. Na_2SO_4 aqueous buffer solutions were prepared adjusted to the pH 3 by titration with H_2SO_4.

The electrochemical setup was coupled to a solar light simulator (Sciencetech; model SLB-300B; 300 W Xe lamp; AM 1.5 global filter) and calibrated to 1 sun (100 mW/cm^2) using a thermopile optical detector (Newport; model 818P-010-12). The PEC water oxidation measurements were conducted in a 0.1 M Na_2SO_4 (pH 3) solution under 1 sun illumination in a three-electrode PEC cell with a 420 nm (λ < 420 nm), 435 nm (λ < 435 nm), and 490 nm (λ < 490 nm) cutoff filter, and experiments using a chopped light were performed using a shutter with a 2-s period.

The current density-voltage (j-V) curves were measured on photoanodes in 0.1 M Na_2SO_4 under dark and light conditions with a scanning rate of 50 mV/s between −0.2 and 1.8 V (versus Ag/AgCl) by the LSV measurements. The potentials were converted to V versus RHE (reversible hydrogen electrode) using the Nernst equation,

$$V_{RHE} = V_{Ag/AgCl}(V) + 0.059 \times pH + V^o_{Ag/AgCl}(V),$$

where V_{RHE} is the applied potential versus RHE; $V_{Ag/AgCl}$ (V) is the applied potential versus Ag/AgCl reference electrode; and $V^o_{Ag/AgCl}$ (V) is the standard potential of the reference electrode (0.197 V_{RHE}).

EIS under light condition was also conducted. EIS spectra were recorded in the frequency range from 100 kHz to 0.1 Hz at a bias of 1.23 V_{RHE} with an alternating current (AC) voltage of 10 mV.

IPCE measurement was obtained by illumination the photoanodes in a three-electrode setup with light from the Xenon lamp was supplied by a monochromator, and the photocurrent was recorded at a constant bias (1.23 V_{RHE}) with a spectral step of 10 nm from 300 nm to 600 nm. This light was entered into a specific monochromator (Oriel 1/8 m cornerstone; 1,200 lines/mm grating), and the output of the monochromator was illuminated into the sample.

The current was recorded using a computer-controlled setup consisting of a potentiostat (CH instrument). The dark and under illumination current values for different incident light wavelengths were measured. To find the portion of the photocurrent, these two current amounts were subtracted. To calculate the IPCE, the following equation was used:

$$IPCE(\%) = \frac{1240}{\lambda} \times \frac{j}{P_{light}} \times 100,$$

where j is the photocurrent density (mA/cm^2), λ is the incident light wavelength (nm) from monochromatic light, and P_{light} is the power density of monochromatic light at a specific wavelength (mW/cm^2). The standard silicon photodiode (Thorlabs) was used to measure the power density of monochromatic light.

Time-resolved fluorescence measurements

Time-resolved fluorescence decays of the dye solutions were acquired by using a PicoHarp 200 time-resolved single photon counting system (PicoQuant). The time-resolved photon count decay curves were recorded at the wavelengths where the emission maxima were observed in the fluorescence measurements. Amplitude-averaged lifetimes were extracted by an exponential reconvolution method using the FluoFit software. A pulsed laser emitting at 495 nm was employed as the excitation source.

Photocatalytic degradation testing

This experiment has been carried out to test the degradation of [SF] and [CoFe–SF]. For this aim, both aqueous solutions are exposed to solar irradiation (1 sun; 100 mW/cm^2) for 500 min in the presence of WO$_3$ ($\sim$2 mg each). The WO$_3$ nano powder was removed from FTO samples using razor blade and then dispersed in 3 mL of 60-μM solutions in quartz cuvettes. During the experiments, composites were at the bottom of the cuvette and hence did not interfere with the data acquisition. At the end of this experiment, the color of the [SF] fades, and its characteristic absorption bands disappear. On the other hand, [CoFe–SF] has much less photodecomposition as a function of exposure time and it still preserves its spectral response.

Ab initio electronic structure calculations

The *ab initio* electronic structure calculations based on density functional theory with periodic boundary conditions implemented in the Vienna *Ab initio* Simulation Package (VASP)[34–37] were performed. The exchange-correlation interaction was described within the Perdew-Burke-Ernzerhof (PBE) scheme of generalized gradient approximation (GGA).[38] The potentials of elements were portrayed with the projected augmented wave (PAW) method,[39] setting a kinetic energy cutoff of 520 eV for the plane-wave basis set. The numerical integrations over the Brillouin zone were calculated at the gamma point. A vacuum space of 15 Å was taken to prevent artificial interactions between periodic images. The structural relaxations were performed by using conjugate gradient optimization allowing 10^{-5} eV energy tolerance between two sequential steps and allowing maximum 0.01 eV/Å force on atoms.

Femtosecond transient absorption spectroscopy measurements

A Ti:sapphire laser amplifier optical parametric amplifier system with 52 fs pulse duration and 1 kHz repetition rate (Spectra Physics; Spitfire Pro XP; TOPAS) and a commercial pump probe experimental setup (Spectra Physics; Helios) with a white light continuum probe was used for the experiments. The pulse duration was measured as 120 fs by cross-correlation inside the pump probe setup. Wavelength of the pump beam was chosen according to the steady-state absorption spectra of

studied compounds. Experimental data were analyzed by using Surface Xplorer software that is supported by Ultrafast Systems.

REFERENCES

1. Ashford, D.L., Gish, M.K., Vannucci, A.K., Brennaman, M.K., Templeton, J.L., Papanikolas, J.M., and Meyer, T.J. (2015). Molecular chromophore-catalyst assemblies for solar fuel applications. Chem. Rev. *115*, 13006–13049.

2. Yu, Z., Li, F., and Sun, L. (2015). Recent advances in dye-sensitized photoelectrochemical cells for solar hydrogen production based on molecular components. Energy Environ. Sci. *8*, 760–775.

3. Wang, D., Niu, F., Mortelliti, M.J., Sheridan, M.V., Sherman, B.D., Zhu, Y., McBride, J.R., Dempsey, J.L., Shen, S., Dares, C.J., et al. (2020). A stable dye-sensitized photoelectrosynthesis cell mediated by a NiO overlayer for water oxidation. Proc. Natl. Acad. Sci. USA *117*, 12564–12571.

4. Li, F., Fan, K., Xu, B., Gabrielsson, E., Daniel, Q., Li, L., and Sun, L. (2015). Organic dye-sensitized tandem photoelectrochemical cell for light driven total water splitting. J. Am. Chem. Soc. *137*, 9153–9159.

5. Son, H.J., Prasittichai, C., Mondloch, J.E., Luo, L., Wu, J., Kim, D.W., Farha, O.K., and Hupp, J.T. (2013). Dye stabilization and enhanced photoelectrode wettability in water-based dye-sensitized solar cells through post-assembly atomic layer deposition of TiO2. J. Am. Chem. Soc. *135*, 11529–11532.

6. Gray, C.L., Xu, P., Rothenberger, A.J., Koehler, S.J., Elacqua, E., Milosavljevic, B.H., and Mallouk, T.E. (2020). Oligomeric ruthenium polypyridyl dye for improved stability of aqueous photoelectrochemical cells. J. Phys. Chem. C *124*, 3542–3550.

7. McCusker, J.K. (2019). Electronic structure in the transition metal block and its implications for light harvesting. Science *363*, 484–488.

8. Kirner, J.T., and Finke, R.G. (2017). Water-oxidation photoanodes using organic light-harvesting materials: A review. J. Mater. Chem. A *5*, 19560–19592.

9. Young, E.R., and Oldacre, A. (2019). Iron hits the mark. Science *363*, 225–226.

10. Wenger, O.S. (2019). Is iron the new ruthenium? Chemistry *25*, 6043–6052.

11. Harlang, T.C.B., Liu, Y., Gordivska, O., Fredin, L.A., Ponseca, C.S., Jr., Huang, P., Chábera, P., Kjaer, K.S., Mateos, H., Uhlig, J., et al. (2015). Iron sensitizer converts light to electrons with 92% yield. Nat. Chem. *7*, 883–889.

12. Braun, J.D., Lozada, I.B., Kolodziej, C., Burda, C., Newman, K.M.E., van Lierop, J., Davis, R.L., and Herbert, D.E. (2019). Iron(II) coordination complexes with panchromatic absorption and nanosecond charge-transfer excited state lifetimes. Nat. Chem. *11*, 1144–1150.

13. Kjær, K.S., Kaul, N., Prakash, O., Chábera, P., Rosemann, N.W., Honarfar, A., Gordivska, O., Fredin, L.A., Bergquist, K.E., Häggström, L., et al. (2019). Luminescence and reactivity of a charge-transfer excited iron complex with nanosecond lifetime. Science *363*, 249–253.

14. Moore, G.F., Blakemore, J.D., Milot, R.L., Hull, J.F., Song, H., Cai, L., Schmuttenmaer, C.A., Crabtree, R.H., and Brudvig, G.W. (2011). A visible light water-splitting cell with a photoanode formed by codeposition of a high-potential porphyrin and an iridium water-oxidation catalyst. Energy Environ. Sci. *4*, 2389–2392.

15. Yamamoto, M., Nishizawa, Y., Chábera, P., Li, F., Pascher, T., Sundström, V., Sun, L., and Imahori, H. (2016). Visible light-driven water oxidation with a subporphyrin sensitizer and a water oxidation catalyst. Chem. Commun. (Camb.) *52*, 13702–13705.

16. Wang, D., Eberhart, M.S., Sheridan, M.V., Hu, K., Sherman, B.D., Nayak, A., Wang, Y., Marquard, S.L., Dares, C.J., and Meyer, T.J. (2018). Stabilized photoanodes for water oxidation by integration of organic dyes, water oxidation catalysts, and electron-transfer mediators. Proc. Natl. Acad. Sci. USA *115*, 8523–8528.

17. Kirner, J.T., Stracke, J.J., Gregg, B.A., and Finke, R.G. (2014). Visible-light-assisted photoelectrochemical water oxidation by thin

films of a phosphonate-functionalized perylene diimide plus CoOx cocatalyst. ACS Appl. Mater. Interfaces 6, 13367–13377.

18. Kirner, J.T., and Finke, R.G. (2017). Sensitization of nanocrystalline metal oxides with a phosphonate-functionalized perylene diimide for photoelectrochemical water oxidation with a CoOx catalyst. ACS Appl. Mater. Interfaces 9, 27625–27637.

19. Ulusoy Ghobadi, T.G., Akhuseyin Yildiz, E., Buyuktemiz, M., Sadigh Akbari, S., Topkaya, D., İsci, Ü., Dede, Y., Yaglioglu, H.G., and Karadas, F. (2018). A noble-metal-free heterogeneous photosensitizer-relay catalyst triad that catalyzes water oxidation under visible light. Angew. Chem. Int. Ed. Engl. 57, 17173–17177.

20. Ulusoy Ghobadi, T.G., Ghobadi, A., Buyuktemiz, M., Yildiz, E.A., Berna Yildiz, D., Yaglioglu, H.G., Dede, Y., Ozbay, E., and Karadas, F. (2020). A robust, precious-metal-free dye-sensitized photoanode for water oxidation: a nanosecond-long excited-state lifetime through a Prussian blue analogue. Angew. Chem. Int. Ed. Engl. 59, 4082–4090.

21. Oshima, T., Nishioka, S., Kikuchi, Y., Hirai, S., Yanagisawa, K.I., Eguchi, M., Miseki, Y., Yokoi, T., Yui, T., Kimoto, K., et al. (2020). An artificial Z-scheme constructed from dye-sensitized metal oxide nanosheets for visible light-driven overall water splitting. J. Am. Chem. Soc. 142, 8412–8420.

22. Aksoy, M., Nune, S.V.K., and Karadas, F. (2016). A novel synthetic route for the preparation of an amorphous Co/Fe Prussian blue coordination compound with high electrocatalytic water oxidation activity. Inorg. Chem. 55, 4301–4307.

23. Shan, B., Brennaman, M.K., Troian-Gautier, L., Liu, Y., Nayak, A., Klug, C.M., Li, T.T., Bullock, R.M., and Meyer, T.J. (2019). A silicon-based heterojunction integrated with a molecular excited state in a water-splitting tandem cell. J. Am. Chem. Soc. 141, 10390–10398.

24. Shan, B., Vanka, S., Li, T.-T., Troian-Gautier, L., Brennaman, M.K., Mi, Z., and Meyer, T.J. (2019). Binary molecular-semiconductor p–n junctions for photoelectrocatalytic CO2 reduction. Nat. Energy 4, 290–299.

25. Hayat, K., Gondal, M.A., Khaled, M.M., Yamani, Z.H., and Ahmed, S. (2011). Laser induced photocatalytic degradation of hazardous dye (Safranin-O) using self synthesized nanocrystalline WO3. J. Hazard. Mater. 186, 1226–1233.

26. Wang, P., Guo, S., Wang, H.-J., Chen, K.-K., Zhang, N., Zhang, Z.-M., and Lu, T.-B. (2019). A broadband and strong visible-light-absorbing photosensitizer boosts hydrogen evolution. Nat. Commun. 10, 3155.

27. Guo, S., Chen, K.-K., Dong, R., Zhang, Z.-M., Zhao, J., and Lu, T.-B. (2018). Robust and long-lived excited state Ru(II) polyimine photosensitizers boost hydrogen production. ACS Catal. 8, 8659–8670.

28. Gish, M.K., Lapides, A.M., Brennaman, M.K., Templeton, J.L., Meyer, T.J., and Papanikolas, J.M. (2016). Ultrafast recombination dynamics in dye-sensitized SnO2/TiO2 core/shell films. J. Phys. Chem. Lett. 7, 5297–5301.

29. Zigler, D.F., Morseth, Z.A., Wang, L., Ashford, D.L., Brennaman, M.K., Grumstrup, E.M., Brigham, E.C., Gish, M.K., Dillon, R.J., Alibabaei, L., et al. (2016). Disentangling the physical processes responsible for the kinetic complexity in interfacial electron transfer of excited Ru(II) polypyridyl dyes on TiO2. J. Am. Chem. Soc. 138, 4426–4438.

30. Bettis, S.E., Hanson, K., Wang, L., Gish, M.K., Concepcion, J.J., Fang, Z., Meyer, T.J., and Papanikolas, J.M. (2014). Photophysical characterization of a chromophore/water oxidation catalyst containing a layer-by-layer assembly on nanocrystalline TiO2 using ultrafast spectroscopy. J. Phys. Chem. A 118, 10301–10308.

31. Jiao, Z., Sun, X.W., Wang, J., Ke, L., and Demir, H.V. (2010). Hydrothermally grown nanostructured WO3 films and their electrochromic characteristics. J. Phys. D Appl. Phys. 43, 285501.

32. Su, J., Feng, X., Sloppy, J.D., Guo, L., and Grimes, C.A. (2011). Vertically aligned WO3 nanowire arrays grown directly on transparent conducting oxide coated glass: synthesis and photoelectrochemical properties. Nano Lett. 11, 203–208.

33. Ghobadi, T.G.U., Ghobadi, A., Soydan, M.C., Vishlaghi, M.B., Kaya, S., Karadas, F., and Ozbay, E. (2020). Strong light-matter interactions in Au plasmonic nanoantennas coupled with Prussian blue catalyst on BiVO4 for photoelectrochemical water splitting. ChemSusChem 13, 2577–2588.

34. Kresse, G., and Furthmüller, J. (1996). Efficient iterative schemes for ab initio total-energy calculations using a plane-wave basis set. Phys. Rev. B Condens. Matter 54, 11169–11186.

35. Kresse, G., and Hafner, J. (1994). Ab initio molecular-dynamics simulation of the liquid-metal-amorphous-semiconductor transition in germanium. Phys. Rev. B Condens. Matter 49, 14251–14269.

36. Kresse, G., and Hafner, J. (1993). Ab initio molecular dynamics for liquid metals. Phys. Rev. B Condens. Matter 47, 558–561.

37. Kresse, G., and Furthmüller, J. (1996). Efficiency of ab-initio total energy calculations for metals and semiconductors using a plane-wave basis set. Comput. Mater. Sci. 6, 15–50.

38. Perdew, J.P., Burke, K., and Ernzerhof, M. (1996). Generalized gradient approximation made simple. Phys. Rev. Lett. 77, 3865–3868.

39. Blöchl, P.E. (1994). Projector augmented-wave method. Phys. Rev. B Condens. Matter 50, 17953–17979.